






Tuning Dzyaloshinskii-Moriya interaction in ferrimagnetic GdCo: A first-principles approach

Md Golam Morshed ^{1,*}, Khoong Hong Khoo,² Yassine Quessab ³, Jun-Wen Xu ³, Robert Laskowski,² Prasanna V. Balachandran,^{4,5} Andrew D. Kent ³ and Avik W. Ghosh ^{1,6}

¹*Department of Electrical and Computer Engineering, University of Virginia, Charlottesville, Virginia 22904, USA*

²*Institute of High Performance Computing, Agency for Science, Technology and Research, 1 Fusionopolis Way, Connexis, Singapore 138632, Singapore*

³*Center for Quantum Phenomena, Department of Physics, New York University, New York, New York 10003, USA*

⁴*Department of Materials Science and Engineering, University of Virginia, Charlottesville, Virginia 22904, USA*

⁵*Department of Mechanical and Aerospace Engineering, University of Virginia, Charlottesville, Virginia 22904, USA*

⁶*Department of Physics, University of Virginia, Charlottesville, Virginia 22904, USA*



(Received 14 January 2021; revised 26 April 2021; accepted 27 April 2021; published 12 May 2021)

We present a systematic analysis of our ability to tune chiral Dzyaloshinskii-Moriya interaction (DMI) in compensated ferrimagnetic Pt/GdCo/Pt_{1-x}W_x trilayers by cap layer composition. Using first-principles calculations, we show that the DMI increases rapidly for only $\sim 10\%$ W and saturates thereafter, in agreement with experiments. The calculated DMI shows a spread in values around the experimental mean, depending on the atomic configuration of the cap layer interface. The saturation is attributed to the vanishing of spin-orbit coupling energy at the cap layer and the simultaneous constancy at the bottom interface. Additionally, we predict the DMI in Pt/GdCo/*X* (*X* = Ta, W, Ir) and find that W in the cap layer favors a higher DMI than Ta and Ir that can be attributed to the difference in *d*-band overlap around the Fermi level. Our results open up exciting combinatorial possibilities for controlling the DMI in ferrimagnets towards nucleating and manipulating ultrasmall high-speed skyrmions.

DOI: [10.1103/PhysRevB.103.174414](https://doi.org/10.1103/PhysRevB.103.174414)

I. INTRODUCTION

Magnetic skyrmions are topologically protected spin textures and are attractive for next-generation spintronic applications, such as racetrack memory and logic devices [1–7]. The interfacial Dzyaloshinskii-Moriya interaction (DMI), an antisymmetric exchange originating from the strong spin-orbit coupling (SOC) in systems with broken inversion symmetry [8,9], is one of the key ingredients in the formation of skyrmions in magnetic multilayers [10–12]. Controlling the DMI offers the possibility to manipulate skyrmion properties, i.e., size and stability [13,14].

Over the past few years, the underlying DMI physics and overall skyrmion dynamics have been studied extensively for ferromagnetic (FM) systems [12,15–20]. Reference [15] reported interfacial DMI in the Pt/Co bilayer with varying thicknesses of Pt and Co layers. A wide range of heavy metals (HMs) with large SOC in proximity to FM layers demonstrated the role of band overlap around the Fermi level in the sign and magnitude of the DMI [16,18]. Moreover, another common approach to produce a net effective DMI is to insert a FM layer between different SOC metals [12,21]. Although both HM/FM bilayers and HM/FM/HM sandwiched structures have been explored, most of the reported results are based on ideal interfaces. Indeed, very few studies focus on the role of disorder in DMI [22]. Furthermore, ferrimagnetic materials have drawn attention due to their low saturation

magnetization, low stray fields, reduced sensitivity to external magnetic fields, and fast spin dynamics, all of which favor ultrafast and ultrasmall skyrmions [23–27]. One prototypical example is GdCo thin films. GdCo is an amorphous alloy with two antiferromagnetically coupled sublattices (Gd and Co) that have different temperature dependences. At the magnetic compensation temperature T_M , the magnetic moments of the two sublattices cancel each other out, and the net GdCo magnetization goes to zero. Very recently, Quessab *et al.* experimentally studied the interfacial DMI in amorphous Pt/GdCo thin films (magnetic compensation of GdCo for $\approx 25\%$ Gd occurs at ~ 150 K) and showed a strong tunability of the DMI by varying the thickness of the GdCo alloy and cap layer composition [28]. However, a detailed understanding of DMI, including the impact of two-sublattice ferrimagnetism, and the role of an experimentally realistic, chemically disordered interface are both missing.

In this paper, we present a systematic theoretical analysis of the DMI in a compensated ferrimagnetic alloy using first-principles calculations. In particular, we explore the variation of the DMI in Pt/GdCo/Pt_{1-x}W_x (Fig. 1) and find a strong tunability from 0 to 4.42 mJ/m² with variation in the W composition (Fig. 2). We studied the influence of atom placement and observed that the DMI is sensitive to structural variations such as the GdCo configuration in the thin magnetic film and the PtW configuration at the interface. This is important to consider because, in reality, we have an amorphous alloy and the interfaces in deposited films are not perfect. We find a spectrum of DMI values that show an overall saturating trend, as seen in the experimental data [28]. We argue that the

*mm8by@virginia.edu

change in SOC energy in the interfacial HM layers, especially the constancy of the SOC energy in the bottom layer and its reduction in the cap layer, generates the observed saturating trend in the DMI with the percentage of W incorporated (Fig. 3). Additionally, we theoretically predict the variation of the DMI depending on the cap layer material, specifically for Pt/GdCo/*X*, where *X* = Ta, W, Ir (Fig. 4). We find that the DMI is highest for W in the cap layer and lowest for Ir, a trend that correlates with *3d-5d* Co-*X* band overlap at the cap layer interface (Fig. 5). Our results identify the chemical and geometric factors responsible for interfacial DMI, and provide a potential path forward towards the engineering of material properties for next-generation skyrmion-based spintronic applications.

II. METHODS

We use the technique of constraining the magnetic moments in a supercell to calculate the DMI within the density functional theory (DFT) framework [15]. The Vienna Ab initio Simulation Package (VASP) is used for the DFT calculations [29]. We use the projector augmented wave potential to describe the core-electron interaction [30,31]. The Perdew-Burke-Ernzerhof (PBE) functional form of the generalized gradient approximation (GGA) is used for the exchange-correlation functional [32]. In order to treat the on-site Coulomb interaction of Gd 4*f* electrons, we use the GGA+*U* method [33] with an effective value of *U* = 6 eV for Gd, as reported in previous studies for both bulk and slab calculations [34–36]. We also validate the effective *U* for our GdCo alloy by taking a range of *U* values from 1 to 7 eV and confirming a stable ferrimagnetic ground-state configuration of GdCo at *U* = 6 eV. A 4 × 1 × 1 supercell of Pt(2)/GdCo(2)/Pt_{1-*x*}W_{*x*}(2) (the numbers in the parentheses represent the number of monolayers) is used in all our calculations. While creating the GdCo alloy by replacing Gd atoms in the hcp Co(0001) slab, a 25% Gd composition is maintained, which is the closest to the experimental proportion (22% Gd [28]) achievable within our structural arrangement. The trilayers are formed by aligning fcc(111) and hcp(0001) planes. The in-plane lattice constant of the slab structure is set to 2.81 Å, equal to the calculated nearest-neighbor distance of bulk Pt, and the supercells are separated by a vacuum layer of 10 Å in the [001] direction. The cutoff energy is set to 500 eV, and a 4 × 16 × 1 Monkhorst-pack *k* grid is used for all the calculations. We verify the convergence of our calculations with cutoff energy, the number of *k* points, and the thickness of the vacuum layer.

The three-step DMI calculation procedure starts with ionic relaxation along the atomic *z* coordinate to mimic a thin film, until the forces become smaller than 0.01 eV/Å and the energy difference between two ionic relaxation steps becomes smaller than 10⁻⁶ eV. Next, in the absence of SOC, the non-spin-polarized Kohn-Sham equations are solved to find an initial charge density. Finally, SOC is included, and the total energy of the system is calculated self-consistently for clockwise (CW) and counterclockwise (CCW) spin configurations (Fig. 1) until the energy difference between two consecutive steps becomes smaller than 10⁻⁶ eV. We consider

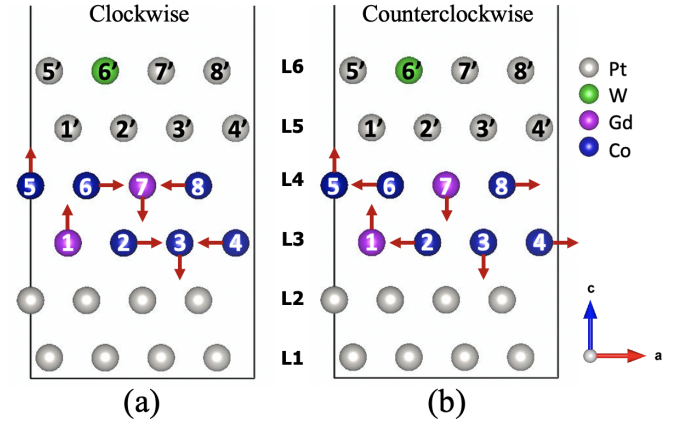


FIG. 1. Schematic of the Pt(2)/GdCo(2)/Pt_{1-*x*}W_{*x*}(2) structure (the number in parentheses denotes the number of monolayers) corresponding to *x* = 12.5% for (a) CW and (b) CCW spin configurations. The red arrows show the spin orientations for noncollinear calculations. Even though we select the FM alignment between atoms at sites 1 and 5 (3 and 7) when constructing the spin spiral, we end up subtracting the energies between CW and CCW spin configurations to obtain the DMI, so this particular interaction cancels out. L1, . . . , L6 denote the layer number, while numbers in circles label atomic positions.

antiferromagnetic coupling between the Gd and Co moment while performing the relaxation and ground-state calculations.

III. RESULTS

The DMI energy E_{DMI} can be defined as

$$E_{DMI} = \sum_{(i,j)} \mathbf{d}_{ij} \cdot (\mathbf{S}_i \times \mathbf{S}_j), \quad (1)$$

where \mathbf{S}_i , \mathbf{S}_j are the nearest-neighbor normalized atomic spins and \mathbf{d}_{ij} is the corresponding DMI vector. The total DMI strength d^{tot} , defined by the summation of the DMI coefficient of each layer, to a first approximation, is calculated by the energy difference between the CW and CCW spin configurations [15] and expressed as $d^{\text{tot}} = (E_{CW} - E_{CCW})/12$. The relation between the d^{tot} that relates the DMI energy to spin configurations and the micromagnetic DMI D that relates the micromagnetic energy per unit volume to magnetization m via the equation $E = D(m_z \partial_x m_x - m_x \partial_x m_z + m_z \partial_y m_y - m_y \partial_y m_z)$ [1] is given by $D = 3\sqrt{2}d^{\text{tot}}/N_F a^2$, where N_F and a represent the number of magnetic layers and the fcc lattice constant, respectively [15]. We take into account both the Co-Co and Co-Gd bond while doing the DMI calculations and report the average DMI per bond.

Before presenting the numerical results, it is worth mentioning that we can investigate only a limited subset of the structures for our calculations, as exploring all combinatorial possibilities is not feasible in terms of time and computational resources. We consider two separate alloy configurations: (i) Gd alloying in the magnetic layers, and (ii) W alloying in the cap layers.

In case (i), we first fix the position of the Gd atoms in the GdCo alloy. We maintain 25% Gd composition separately in each magnetic layer, arguing that steric repulsion implies two Gd atoms are energetically unlikely to sit in the same

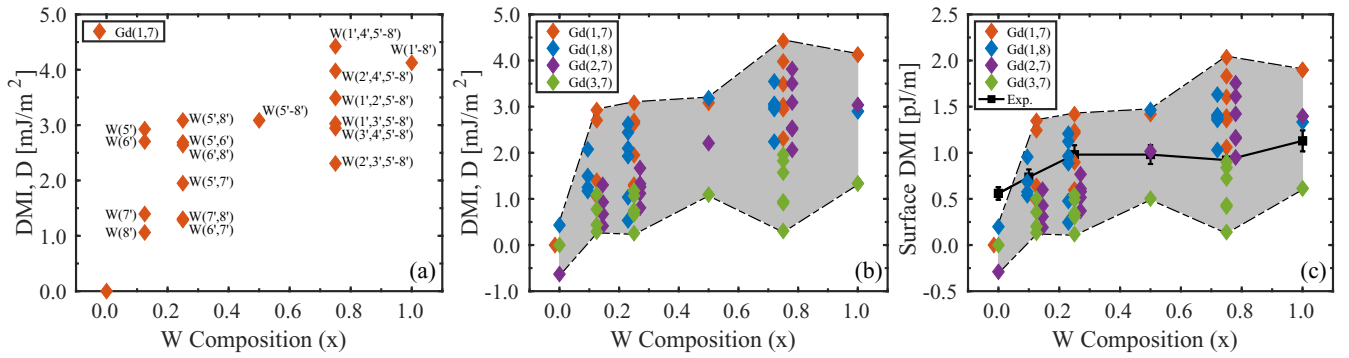


FIG. 2. The DMI as a function of W composition x in Pt/GdCo/Pt $_{1-x}$ W $_x$. (a) DMI variation with respect to W positions while the Gd atoms are fixed at (1,7) positions. (b) Total spectrum of the DMI as both Gd and W positions are varied. For a specific W composition, each of the different colors represents the variation of Gd atomic positions, and the scattered points within the same color represent different W positions for that particular Gd arrangement in the structure (Fig. 1). (c) Surface DMI in comparison with experimentally observed DMI [28]. The numbers followed by the symbols Gd and W represent the positions of the respective atoms in the structure shown in Fig. 1.

layer, as assumed in previous studies [37]. The Gd atoms can thus arrange themselves in $\binom{4}{1} \times \binom{4}{1} = 16$ ways. These 16 combinations can be grouped into just four distinct sets because of their translational symmetry. In Fig. 1, looking at positions 1–8 in magnetic layers L3 and L4, it can be seen that Gd atoms in the (1, 7), (2, 8), (3, 5), and (4, 6) positions represent equivalent structures once the unit cell is periodically extended. Similarly, the other three groups are [(1, 8), (2, 5), (3, 6), (4, 7)], [(1, 6), (2, 7), (3, 8), (4, 5)], and [(1, 5), (2, 6), (3, 7), (4, 8)]. We confirmed this equivalence by calculating the energy of the Pt/GdCo stack by varying all the Gd positions and, indeed, find equal energy for the four structures within the same group. For case (ii), we choose one representative from each of the above four groups and proceed with W positional variations in the cap layer. While exploring W alloy configurations, for lower composition (12.5%–50%), W is incorporated in only layer L6. Finally, we vary all the possible W positions and calculate the DMI for a total of 76 structures.

Figure 2(a) shows the calculated DMI D for Pt/GdCo/Pt $_{1-x}$ W $_x$ as a function of W composition. At $x = 0\%$, the DMI vanishes as expected because, for a perfectly symmetric trilayer structure, the contributions from the bottom and top interfaces are equal and opposite. As the W composition increases from 0% to 12.5%, we find a maximum DMI of 2.93 mJ/m 2 . The underlying mechanism behind this nonzero DMI is the symmetry breaking of the Pt/GdCo/Pt structure by the insertion of W atoms in the cap layer. When a W atom is included in the cap layer, the overall symmetry of the stack is broken, but it still leaves intact the mirror symmetry with the normal of the symmetry plane parallel to the b axis (Fig. 1), and hence by the Moriya rules [9], we get the D vector parallel to b axis. We find that a small amount of W (12.5%) gives a large DMI change, and subsequent to that initial rise, with increasing W content, the DMI saturates. As the composition of W increases, we find a maximum DMI of 4.42 mJ/m 2 , corresponding to 75% W composition.

We find that the DMI is very sensitive to the structural details, specifically the positions of the Gd and W atoms. Figure 2(a) shows the variation of D as the position of the W atoms changes. In Fig. 2(a), for all cases, Gd atoms are fixed at

the (1,7) positions. We show the variation of W positions for the structures with the 12.5%, 25%, and 75% compositions because for the other three cases there is only one combination possible in terms of W positions. Figure 2(b) shows the total spectrum of the DMI variation while varying both the Gd and W positions in the structure. Interestingly, for all the cases, the increasing trend of the DMI is very similar. We conjecture that changing the position of the atoms within the small unit cell will change the nature of the interface that gives variations in the DMI. For example, in the case of Pt/GdCo/W, when Gd atoms are placed at position (1, 7), the SOC energy change in the interfacial Pt layer is higher than that of position (3, 7), which translates to the corresponding DMI as well.

To validate our results against the recent experiment [28], we calculate the surface DMI (in units of picojoules per meter) by multiplying the calculated DMI D by the thickness of the magnetic layers. In our calculations, we use the thickness $N_F a / \sqrt{3} = 4.6 \text{ \AA}$ for the magnetic layers, while the experimental thickness is 5 nm. Figure 2(c) shows the surface DMIs from both the DFT calculation and the experiment, scaled by their respective thicknesses. In the experiment, a nonzero DMI of 0.56 pJ/m (solid black line) is found for the Pt/GdCo/Pt structure because of the asymmetry in the bottom and top interfaces due to the difference in interface roughness and intermixing [28]. On the contrary in our DFT model, we use a perfect crystal structure that gives a nearly zero DMI for the symmetric cases (a small nonzero DMI might arise from intrinsic asymmetry within a thin crystalline GdCo film modeled here). We find an overall matching trend between the DFT and experimental data for the rest of the compositions. An exact quantitative agreement between the DFT results and the experiment is difficult to achieve because we use a crystal structure for our model, whereas, in the experiment, amorphous or polycrystalline materials are used. Additionally, the magnetization also differs between our model and the experiment as the thicknesses and the dimensions of the structure are different. However, we argue that the structural imperfections in the experiment amount to an ensemble averaging over the various configurations we theoretically explore, so that the experimental data fall in the middle of the spectrum (gray shaded area) of our DFT data.

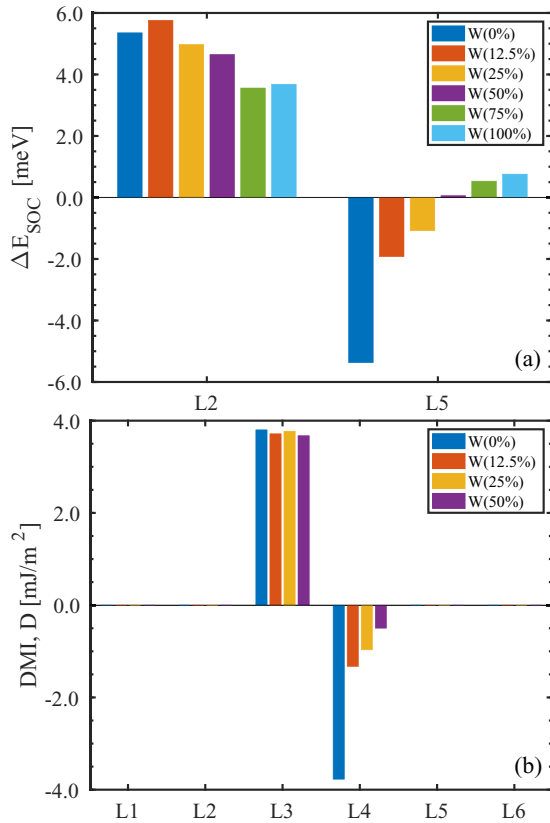


FIG. 3. (a) Change in SOC energy at the interfacial HM layers (L2 and L5) as a result of changing spin chirality of the magnetic layers (L3 and L4) from CW to CCW. All the color bars on the left (right) side represent the SOC energy change at L2 (L5) for different W compositions. (b) Layer-resolved DMI for structures with W composition $x = 0\%$ – 50% .

In Fig. 2, the DMI increases in a nonlinear fashion as a function of W composition as opposed to the linear increase one may expect. This nonlinear trend can be explained by the change in spin-orbit coupling energy ΔE_{SOC} in the HM layers adjacent to the magnetic layers in Fig. 1. ΔE_{SOC} is defined by the change in SOC energy as the spin orientation changes from CW to CCW at the magnetic layers (L3 and L4 in Fig. 1). In Fig. 3(a), we show ΔE_{SOC} per atom in L2 (adjacent to the bottom magnetic layer) and L5 (adjacent to the top magnetic layer) for all W compositions (0%–100%). We find that ΔE_{SOC} in L5 changes drastically as W composition changes from 0% to 12.5%, slowing down thereafter. On the other hand, distributions of ΔE_{SOC} in L2 are not very sensitive to the W composition. Although we find a relatively lower ΔE_{SOC} at L2 for 75% and 100% W compositions, the corresponding ΔE_{SOC} 's at L5 are positive. In trilayer structures, the DMIs of the bottom and top interfaces are additive [12,21], so that the sum arising from L2 and L5 accounts for the observed nonlinear change in DMI in Fig. 2. From our findings, we conjecture that the symmetry breaking plays a vital role in the DMI, while the effect of W composition is not that prominent, in agreement with the recent experiment [28].

To corroborate our analysis, we calculate the layer-resolved DMI contribution from a single layer by changing the spin orientation of that particular layer of interest from

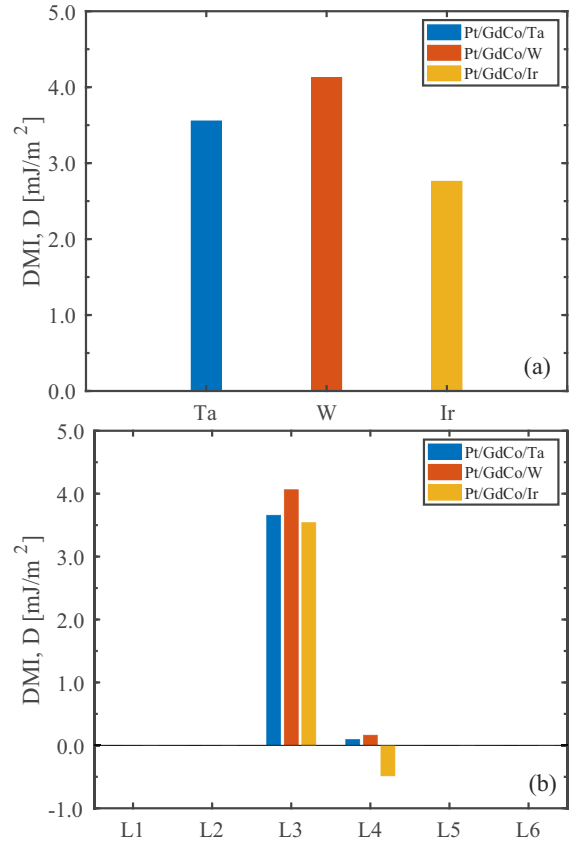


FIG. 4. (a) Calculated DMI in Pt/GdCo/X, where $X = \text{Ta, W, Ir}$. (b) Layer-resolved DMI.

CW to CCW while the spins of all the other layers remain in the original ground-state configuration [15]. For instance, when we calculate the DMI contribution of L3 (Fig. 1), we change only the spin orientation of L3 from CW to CCW (along x and z), and we constrain the spins of all other layers along y , keeping the antiferromagnetic ground-state coupling between Gd and Co magnetic moments. Figure 3(b) shows the layer-resolved contribution of the DMI for the structures with 0%–50% W composition. The results show that the DMI comes only from the interfacial magnetic layers. We can see that the change in the DMI contribution from the top interfacial layer (L4) with increasing W is small, generating a trend similar to ΔE_{SOC} shown in Fig. 3(a). Additionally, the contribution from the bottom interfacial layer (L3) remains almost the same throughout the range of W compositions. The addition of the DMI from the bottom and top interfaces produces a saturation in the overall DMI curve.

Finally, our theoretical model allows us to explore the tuning of DMI in ferrimagnetic systems with different cap layer compositions, which could be critical in designing suitable materials for hosting ultrasmall high-speed skyrmions. Furthermore, for applications, skyrmions can be driven by current-induced spin-orbit torque (SOT) [38]. Changing the cap layer HM offers the ability to tune the SOT efficiency and DMI simultaneously. We report the DMI of Pt/GdCo/X, where $X = \text{Ta, W, Ir}$, to demonstrate the effect of the cap layer $5d$ transition HM on the DMI in Fig. 4(a). We choose the cap layer to be Ta, W, or Ir to maximize the SOT efficiency

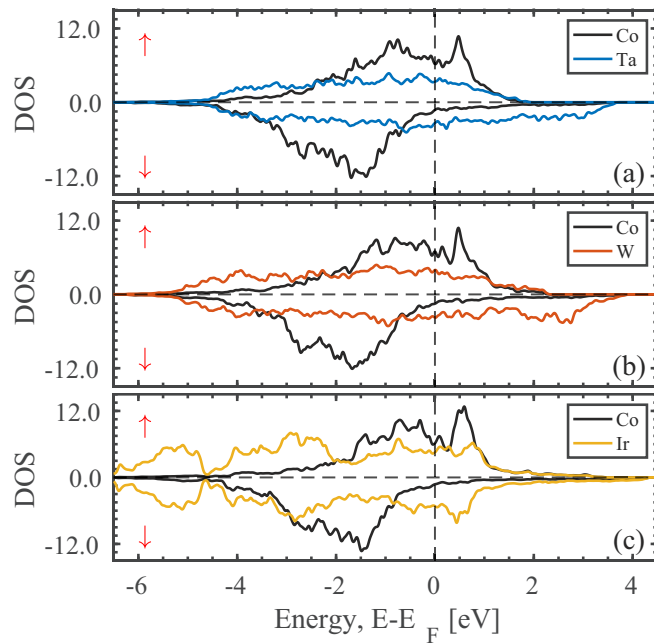


FIG. 5. Projected density of states (DOS) showing the $3d-5d$ band overlap between Co (black) and X (colored) in Pt/GdCo/ X . (a) $X = \text{Ta}$, (b) $X = \text{W}$, and (c) $X = \text{Ir}$. The red up (down) arrow represents the spin-up (spin-down) channel.

for fast and energy-efficient current-induced dynamics in addition to tuning the DMI. W and Ta are known for their giant spin-Hall angle [39,40], and previous studies have shown an additive DMI for a ferromagnet sandwiched between Pt and Ir [11,21], which motivates us to explore these structures and see which one of them has the largest DMI. Moreover, recently, our collaborators reported higher SOT efficiency in Pt/GdCo/W than Pt/GdCo/Ta or Ir [41]. We find that W in the cap layer favors higher DMI than Ta and Ir. To explain the DMI trend, we calculate the layer-resolved DMI contribution from bottom and top interfaces, as shown in Fig. 4(b). From Fig. 4(b), we can observe that the DMI contribution from the top interface (L4) is large when Ir is used as a cap layer material while the DMI contributions are smaller for the cases of W and Ta. The observed trend of the DMI can be explained qualitatively by the Co $3d-X$ $5d$ band overlap, which controls the corresponding orbital hybridization. Figure 5 shows the projected density of states of Co $3d$ and HM $5d$ orbitals. Clearly, in Co/Ir, the band overlap around the Fermi level is higher than that of Co/W and Co/Ta, which in turn produce

larger DMI contributions from L4 for Ir over W and Ta. The band overlaps of Co/W and Co/Ta are close to each other. However, we note that the sign of the DMI contribution from the top interface is different for Ir than Ta and W. By analyzing the atom-resolved orbital projected density of states of the cap layer HM, we find that for Ta and W, d_{xy} and $d_{x^2-y^2}$ are the major contributors near the Fermi level, while d_{xz} and d_{yz} have the smallest contributions. On the other hand, for Ir, d_{xz} and d_{yz} have significant contributions near the Fermi level. We correlate this behavior with the DMI contribution from L4 [Fig. 4(b)], i.e., the Ir $5d$ states near the Fermi level contribute differently than Ta and W, which translate qualitatively into the DMI behavior from the magnetic layer adjacent to the cap layers. Moreover, the variation of the DMI sign depending on the adjacent HM has previously been seen in both theoretical and experimental studies [16,42]. Finally, adding the DMI contribution from both the interfaces [Fig. 4(b)] gives a smaller overall DMI for Pt/GdCo/Ir because of the large negative contribution from the top interface.

IV. CONCLUSION

In summary, we demonstrated the impact of W composition in the cap layer of Pt/GdCo/Pt $_{1-x}$ W $_x$ trilayer structures using first-principles calculations. We found excellent tunability of the DMI that shows a tendency of saturation with increasing W composition. The saturating trend of the DMI is attributed to the change in SOC energy at the top and bottom interfacial HM layers as a function of W composition. Moreover, we found DMI sensitivity to the structural variation. We also demonstrated the DMI variation in Pt/GdCo/(Ta, W, or Ir). We found W in the cap layer provides a higher DMI than Ta and Ir due to the varying degree of orbital hybridization controlled by the band overlap between $3d$ and $5d$ orbitals at the cap layer interface. Our results provide critical insights to the control mechanism of DMI in ferrimagnetic GdCo-based systems, providing a path towards manipulating skyrmion properties for spintronic applications.

ACKNOWLEDGMENTS

We thank S. Gangopadhyay, J. Ma, H. Vakilitaleghani, and S. J. Poon for insightful discussions. This work is funded by the DARPA Topological Excitations in Electronics (TEE) program (Grant No. D18AP00009). The calculations are done using the computational resources from High-Performance Computing systems at the University of Virginia (Rivanna) and XSEDE.

[1] A. Fert, N. Reyren, and V. Cros, *Nat. Rev. Mater.* **2**, 17031 (2017).
 [2] A. Fert, V. Cros, and J. Sampaio, *Nat. Nanotechnol.* **8**, 152 (2013).
 [3] W. Koshibae, Y. Kaneko, J. Iwasaki, M. Kawasaki, Y. Tokura, and N. Nagaosa, *Jpn. J. Appl. Phys.* **54**, 053001 (2015).
 [4] X. Zhang, M. Ezawa, and Y. Zhou, *Sci. Rep.* **5**, 9400 (2015).

[5] H. Vakili, Y. Xie, and A. W. Ghosh, *Phys. Rev. B* **102**, 174420 (2020).
 [6] H. Vakili, M. N. Sakib, S. Ganguly, M. Stan, M. W. Daniels, A. Madhavan, M. D. Stiles, and A. W. Ghosh, *IEEE J. Explor. Solid-State Comput. Devices Circuits* **6**, 107 (2020).
 [7] M. N. Sakib, H. Vakili, S. Ganguly, S. Mosanu, A. W. Ghosh, and M. Stan, *Proc. SPIE* **11470** (Spintronics XIII), 114703D (2020).

- [8] I. Dzyaloshinsky, *J. Phys. Chem. Solids* **4**, 241 (1958).
- [9] T. Moriya, *Phys. Rev.* **120**, 91 (1960).
- [10] S. Heinze, K. von Bergmann, M. Menzel, J. Brede, A. Kubetzka, R. Wiesendanger, G. Bihlmayer, and S. Blügel, *Nat. Phys.* **7**, 713 (2011).
- [11] C. Moreau-Luchaire, C. Moutafis, N. Reyren, J. Sampaio, C. A. F. Vaz, N. Van Horne, K. Bouzehouane, K. Garcia, C. Deranlot, P. Warnicke, P. Wohlhüter, J.-M. George, M. Weigand, J. Raabe, V. Cros, and A. Fert, *Nat. Nanotechnol.* **11**, 444 (2016).
- [12] A. Soumyanarayanan, M. Raju, A. L. Gonzalez Oyarce, A. K. C. Tan, M.-Y. Im, A. P. Petrović, P. Ho, K. H. Khoo, M. Tran, C. K. Gan, F. Ernult, and C. Panagopoulos, *Nat. Mater.* **16**, 898 (2017).
- [13] X. S. Wang, H. Y. Yuan, and X. R. Wang, *Commun. Phys.* **1**, 31 (2018).
- [14] J. Sampaio, V. Cros, S. Rohart, A. Thiaville, and A. Fert, *Nat. Nanotechnol.* **8**, 839 (2013).
- [15] H. Yang, A. Thiaville, S. Rohart, A. Fert, and M. Chshiev, *Phys. Rev. Lett.* **115**, 267210 (2015).
- [16] A. Belabbes, G. Bihlmayer, F. Bechstedt, S. Blügel, and A. Manchon, *Phys. Rev. Lett.* **117**, 247202 (2016).
- [17] V. Kashid, T. Schena, B. Zimmermann, Y. Mokrousov, S. Blügel, V. Shah, and H. G. Salunke, *Phys. Rev. B* **90**, 054412 (2014).
- [18] P. Jadaun, L. F. Register, and S. K. Banerjee, *npj Comput. Mater.* **6**, 88 (2020).
- [19] O. Boulle, J. Vogel, H. Yang, S. Pizzini, D. de Souza Chaves, A. Locatelli, T. O. Menteş, A. Sala, L. D. Buda-Prejbeanu, O. Klein, M. Belmeguenai, Y. Roussigné, A. Stashkevich, S. M. Chérif, L. Aballe, M. Foerster, M. Chshiev, S. Auffret, I. M. Miron, and G. Gaudin, *Nat. Nanotechnol.* **11**, 449 (2016).
- [20] S. Tacchi, R. E. Troncoso, M. Ahlberg, G. Gubbiotti, M. Madami, J. Åkerman, and P. Landeros, *Phys. Rev. Lett.* **118**, 147201 (2017).
- [21] H. Yang, O. Boulle, V. Cros, A. Fert, and M. Chshiev, *Sci. Rep.* **8**, 12356 (2018).
- [22] B. Zimmermann, W. Legrand, D. Maccariello, N. Reyren, V. Cros, S. Blügel, and A. Fert, *Appl. Phys. Lett.* **113**, 232403 (2018).
- [23] S. A. Siddiqui, J. Han, J. T. Finley, C. A. Ross, and L. Liu, *Phys. Rev. Lett.* **121**, 057701 (2018).
- [24] L. Caretta, M. Mann, F. Büttner, K. Ueda, B. Pfau, C. M. Günther, P. Helsing, A. Churikova, C. Klose, M. Schneider, D. Engel, C. Marcus, D. Bono, K. Bagschik, S. Eisebitt, and G. S. D. Beach, *Nat. Nanotechnol.* **13**, 1154 (2018).
- [25] C. T. Ma, Y. Xie, H. Sheng, A. W. Ghosh, and S. J. Poon, *Sci. Rep.* **9**, 9964 (2019).
- [26] D.-H. Kim, M. Haruta, H.-W. Ko, G. Go, H.-J. Park, T. Nishimura, D.-Y. Kim, T. Okuno, Y. Hirata, Y. Futakawa, H. Yoshikawa, W. Ham, S. Kim, H. Kurata, A. Tsukamoto, Y. Shiota, T. Moriyama, S.-B. Choe, K.-J. Lee, and T. Ono, *Nat. Mater.* **18**, 685 (2019).
- [27] S. J. Poon and C. T. Ma, *J. Supercond. Novel Magn.* **33**, 269 (2020).
- [28] Y. Quessab, J.-W. Xu, C. T. Ma, W. Zhou, G. A. Riley, J. M. Shaw, H. T. Nembach, S. J. Poon, and A. D. Kent, *Sci. Rep.* **10**, 7447 (2020).
- [29] G. Kresse and J. Furthmüller, *Phys. Rev. B* **54**, 11169 (1996).
- [30] P. E. Blöchl, *Phys. Rev. B* **50**, 17953 (1994).
- [31] G. Kresse and D. Joubert, *Phys. Rev. B* **59**, 1758 (1999).
- [32] J. P. Perdew, K. Burke, and M. Ernzerhof, *Phys. Rev. Lett.* **77**, 3865 (1996).
- [33] V. I. Anisimov, F. Aryasetiawan, and A. I. Lichtenstein, *J. Phys.: Condens. Matter* **9**, 767 (1997).
- [34] A. B. Shick, W. E. Pickett, and C. S. Fadley, *Phys. Rev. B* **61**, R9213 (2000).
- [35] P. Kurz, G. Bihlmayer, and S. Blügel, *J. Phys.: Condens. Matter* **14**, 6353 (2002).
- [36] M. Petersen, J. Hafner, and M. Marsman, *J. Phys.: Condens. Matter* **18**, 7021 (2006).
- [37] T. Nozaki, A. Koziol-Rachwał, M. Tsujikawa, Y. Shiota, X. Xu, T. Ohkubo, T. Tsukahara, S. Miwa, M. Suzuki, S. Tamaru, H. Kubota, A. Fukushima, K. Hono, M. Shirai, Y. Suzuki, and S. Yuasa, *NPG Asia Mater.* **9**, e451 (2017).
- [38] S. Woo, K. M. Song, H.-S. Han, M.-S. Jung, M.-Y. Im, K.-S. Lee, K. S. Song, P. Fischer, J.-I. Hong, J. W. Choi, B.-C. Min, H. C. Koo, and J. Chang, *Nat. Commun.* **8**, 1 (2017).
- [39] C.-F. Pai, L. Liu, Y. Li, H. W. Tseng, D. C. Ralph, and R. A. Buhrman, *Appl. Phys. Lett.* **101**, 122404 (2012).
- [40] L. Liu, C.-F. Pai, Y. Li, H. W. Tseng, D. C. Ralph, and R. A. Buhrman, *Science* **336**, 555 (2012).
- [41] Q. Yassine, J.-W. Xu, M. G. Morshed, A. W. Ghosh, and A. D. Kent (unpublished).
- [42] X. Ma, G. Yu, C. Tang, X. Li, C. He, J. Shi, K. L. Wang, and X. Li, *Phys. Rev. Lett.* **120**, 157204 (2018).